

Realizing the classical XY Hamiltonian in polariton simulators

Natalia G. Berloff^{1,2,*}, Matteo Silva³, Kirill Kalinin¹, Alexis Askitopoulos³, Julian D. Töpfer³, Pasquale Cilibrizzi³, Wolfgang Langbein⁴ and Pavlos G. Lagoudakis^{1,3*}

¹*Skolkovo Institute of Science and Technology Novaya St.,
100, Skolkovo 143025, Russian Federation*

²*Department of Applied Mathematics and Theoretical Physics,
University of Cambridge, Cambridge CB3 0WA, United Kingdom*

³*Department of Physics and Astronomy, University of Southampton,
Southampton, SO17 1BJ, United Kingdom and*

⁴*School of Physics and Astronomy, Cardiff University,
The Parade, Cardiff CF24 3AA, United Kingdom*

(Dated: July 3, 2017)

Abstract

Several platforms are currently being explored for simulating physical systems, whose complexity increases faster than polynomially with the number of particles or degrees of freedom in the system. Many of these computationally intractable problems can be mapped into classical spin models, such as the Ising and the XY models and be simulated by a suitable physical system. Here, we investigate the potential of polariton graphs as an efficient simulator for finding the global minimum of the classical XY Hamiltonian. By imprinting polariton condensate lattices of bespoke geometries we show that we can simulate a large variety of systems undergoing the $U(1)$ symmetry breaking transitions. We realise various magnetic phases, such as ferromagnetic, anti-ferromagnetic, and frustrated spin configurations on a linear Ising chain, the unit cells of square and triangular lattices, a disordered graph, and demonstrate the potential for size scalability on an extended square lattice of 45 coherently coupled polariton condensates. Our results provide a route to study unconventional superfluids, spin-liquids, Berezinskii-Kosterlitz-Thouless phase transition, and classical magnetism among the many systems that are described by the XY Hamiltonian.

*correspondence address: n.g.berloff@damtp.cam.ac.uk, pavlos.lagoudakis@soton.ac.uk

Social and natural sciences are dominated by systems with many interacting degrees of freedom that operate with a large number of parameters that characterize the state of the system and grow exponentially with system size. Protein folding [1], behaviour of financial markets [2], dynamics of neural networks [3], behaviour of multi-agent systems [4], devising new chemical materials [5], finding the ground state of spin liquids [6] – the list of hard computational problems that modern classical computers cannot tackle for sufficiently large system sizes is large and growing. Recently, it was shown that a large variety of such computationally intractable systems can be mapped into certain universal classical spin models that are characterised by the given degrees of freedom, “spins”, by their interactions, “couplings”, and by the associated cost function, “Hamiltonian” [7]. Depending on the sign, geometry and symmetries of the couplings the problem of finding the global minimum of the associated cost function can be in class P, NP or NP-hard [8, 9]. Finding the global minimum of some classical spin models is known to be NP-complete [10], which means every other problem in NP can be efficiently transformed into it. As a result there has been much interest recently in the possibility of devising a physical system, an analogue simulator, to solve such spin models – n -vector models of classical unit vector spins \mathbf{s}_i with the Hamiltonian $\mathcal{H} = -\sum_{ij} J_{ij} \mathbf{s}_i \cdot \mathbf{s}_j$, where J_{ij} are real numbers specifying the coupling strengths between the sites labelled i and j [11]. The Ising model corresponds to the $n = 1$ case of the n -vector model, with $\mathbf{s}_i \in \{-1, 1\}$. For $n = 2$ the n -vector Hamiltonian becomes $\mathcal{H}_{XY} = -\sum_{ij} J_{ij} \cos(\theta_i - \theta_j)$, where we have parameterized unit planar vectors using the polar coordinates $\mathbf{s}_i = (\cos \theta_i, \sin \theta_i)$. The mapping of the XY model into a universal spin model has been rigorously established [7]. Replacing the unit vectors in the XY Hamiltonian with complex numbers $z_j = \cos \theta_j + i \sin \theta_j$ leads to formulation as the continuous complex constant modulus quadratic optimization problem [12, 13], that is known to be NP-hard in general. The interest in simulating the XY model also comes from the property of \mathcal{H}_{XY} to be invariant under rotation of all spins by the same angle $\theta_i \rightarrow \theta_i + \phi$, therefore, the XY model is the simplest model that undergoes the $U(1)$ symmetry-breaking transition. As such, it is used to emulate other systems featuring a similar broken-symmetry transition whether or not the system is quantum or classical such as the Berezinskii-Kosterlitz-Thouless phase transition and the emergence of a topological order [14, 15], unconventional superfluids and spin-liquid phases.

In this Article, we propose and experimentally demonstrate the use of polariton graphs

as a scheme for finding the global minimum of the classical XY Hamiltonian. Polaritons are the mixed light-matter quasi-particles that are formed in the strong exciton-photon coupling regime in semiconductor microcavities [16]. Under non-resonant optical excitation, rapid relaxation of carriers and bosonic stimulation result in the formation of a non-equilibrium polariton condensate characterized by a single many-body wave-function [17]. Polariton condensates can be imprinted into any two-dimensional graph by spatial modulation of the pumping source, offering straightforward scalability. Optically injected polariton condensates can potentially be imprinted in multi-site configurations with arbitrary polarisation and density profiles offering unprecedented control of the interactions between sites. Due to finite cavity lifetimes, polaritons decay in the form of photons that carry all the information of the corresponding polariton state (energy, momentum, spin and phase) enabling in-situ characterisation of static polariton graphs.

In a graph of two or more coupled polariton vertices, with increasing excitation density, polariton condensation occurs at the state with the phase configuration that carries the highest polariton occupation [18]. This is due to the bosonic character of the condensate formation: the probability of a particle to relax in a particular state grows with the population of that state. At condensation threshold a macroscopic coherent state is formed described by the wavefunction Ψ_g . To the leading order, Ψ_g can be written as a superposition of the wavefunctions Ψ_j at the sites \mathbf{x}_j with phases θ_j ; that is $\Psi_g \approx \sum_j \Psi_j \exp[i\theta_j]$. Below we will show that the system of an arbitrary polariton graph condenses into the global minimum of the XY Hamiltonian: $\mathcal{H}_{XY} = -\sum J_{ij} \cos \theta_{ij}$, where θ_{ij} is the phase difference between two sites, $\theta_{ij} = \theta_i - \theta_j$, and J_{ij} is the corresponding coupling strength; the latter depends on the density of the sites i and j , the distance between them, $d_{ij} = |\mathbf{r}_i - \mathbf{r}_j|$, and the outflow condensate wavenumber k_c , which under non-resonant optical excitation depends on the pumping intensity and profile. The bottom-up approach for the search of the global minimum of the XY Hamiltonian is achievable within the linewidth of the corresponding state. This is an advantage over classical or quantum annealing techniques, where the global ground state is reached through transitions over metastable excited states (local minima), with an increase of the cost of the search with the size of the system.

Modelling the phase coupling: we model the phase coupling in polariton graphs using the complex Ginzburg-Landau equation (cGLE) with a saturable nonlinearity and energy

relaxation [19, 20]:

$$i\hbar\frac{\partial\psi}{\partial t} = -\frac{\hbar^2}{2m}(1-i\eta_d\mathcal{R})\nabla^2\psi + U_0|\psi|^2\psi + \hbar g_R\mathcal{R}\psi + \frac{i\hbar}{2}\left(R_R\mathcal{R} - \gamma_C\right)\psi, \quad (1)$$

$$\frac{\partial\mathcal{R}}{\partial t} = -(\gamma_R + R_R|\psi|^2)\mathcal{R} + P(\mathbf{r}), \quad (2)$$

where ψ is the condensate wavefunction, \mathcal{R} is the density profile of the hot exciton reservoir, m is the polariton effective mass, U_0 and g_R are the strengths of effective polariton-polariton interaction and the blue-shift due to interactions with non-condensed particles, respectively, R_R is the rate at which the exciton reservoir feeds the condensate, γ_C is the decay rate of condensed polaritons, γ_R is the rate of redistribution of reservoir excitons between the different energy levels, η_d is the energy relaxation coefficient specifying the rate at which gain decreases with increasing energy, and P is the pumping into the exciton reservoir. We non-dimensionalize these equations using $\psi \rightarrow \sqrt{\hbar^2/2mU_0\ell_0^2}\psi$, $\mathbf{r} \rightarrow \ell_0\mathbf{r}$, $t \rightarrow 2mt\ell_0^2/\hbar$ and introducing the notations $g = 2g_R/R_R$, $\gamma = m\gamma_C\ell_0^2/\hbar$, $p = m\ell_0^2R_RP(\mathbf{r})/\hbar\gamma_R$, $\eta = \eta_d\hbar/mR_R\ell_0^2$, and $b = R_R\hbar^2/2m\ell_0^2\gamma_RU_0$. We choose $\ell_0 = 1\mu m$ and consider the stationary states.

By using the Madelung transformation $\Psi = \sqrt{\rho}\exp[iS]$ in the dimensionless Eqs. (1,2), where $\rho = |\Psi|^2$, $\mathbf{u} = \nabla S$ is the velocity, S is the phase and separating the real and imaginary parts we obtain the mass continuity and the integrated form of the Bernoulli equation which we write for a steady state, and, therefore, introduce the chemical potential μ

$$\mu = -\frac{\nabla^2\sqrt{\rho}}{\sqrt{\rho}} + \mathbf{u}^2 + \rho + \frac{p(\mathbf{r})}{1+b\rho}\left(g - \eta\frac{\nabla\cdot(\rho\mathbf{u})}{\rho}\right), \quad (3)$$

$$\frac{\nabla\cdot(\rho\mathbf{u})}{\rho} = \frac{p(\mathbf{r})}{1+b\rho}\left(1 + \eta\left(\frac{\nabla^2\sqrt{\rho}}{\sqrt{\rho}} - \mathbf{u}^2\right)\right) - \gamma. \quad (4)$$

First, we consider a single pumping spot with a radially symmetric pumping profile. Asymptotics at large distances from the center of the pump gives the velocity $|u| = k_c = \text{const}$ and $\rho \sim \exp[-\gamma r k_c^{-1}]r^{-1}$. From Eq. (3) at infinity, therefore, we obtain $\mu = k_c^2 - \gamma^2/4k_c^2$. We can estimate the chemical potential for a wide pumping spot so that the quantum pressure term $\nabla^2\sqrt{\rho}/\sqrt{\rho}$ and u_r are insignificant at the pumping center. Under this assumption $\rho_{\max} \approx (p_{\max} - 1)/b$ and $\mu \approx (p_{\max} - 1)/b + g$. Using the asymptotics of the density at infinity and at the center of the pumping spot we can further approximate the density of

the individual pumping spot as

$$\rho(r) \approx \frac{\xi_0}{\xi_1 + \xi_2 r + \xi_3 r^3 + k_c^{-1} r \exp[\gamma r k_c^{-1}]}, \quad (5)$$

where the parameters ξ_i are defined by the pumping profile. In [18] we established experimentally under pulsed excitation that the coupling between two pumping spots (a “polariton dyad”) can be either in-phase or with a π phase difference depending on the outflow wavenumber k_c and the distance between the spots. Below, in the steady state excitation regime, we obtain a general criterion for the switching between the relative phases. We start by considering the wavefunction of the condensate Ψ_g as the sum of the wavefunctions of l_N individual condensates, $\Psi(r) \approx \sqrt{\rho(r)} \exp[ik_c r]$, located at $\mathbf{r} = \mathbf{r}_i$ with the phases θ_i : $\Psi_g(\mathbf{r}) \approx \sum_{i=1}^{l_N} \Psi(|\mathbf{r} - \mathbf{r}_i|) \exp(i\theta_i)$. To find the total amount of matter N we write:

$$N = \int |\Psi_g|^2 d\mathbf{r} = \frac{1}{(2\pi)^2} \int |\widehat{\Psi}_g(\mathbf{k})|^2 d\mathbf{k}, \quad (6)$$

$$\begin{aligned} \widehat{\Psi}_g(\mathbf{k}) &= \int \exp(-i\mathbf{k} \cdot \mathbf{r}) \Psi_g(\mathbf{r}) d\mathbf{r} = \\ &= \widehat{\Psi}(k) \sum_{i=1}^{l_N} \exp(i\mathbf{k} \cdot \mathbf{r}_i + i\theta_i), \end{aligned} \quad (7)$$

where $\widehat{\Psi}(k) = 2\pi \int_0^\infty \Psi(r) J_0(kr) r dr$ and J_0 is the Bessel function. The total amount of matter becomes

$$N = l_N N_0 + \sum_{i < j} J_{ij} \cos(\theta_i - \theta_j), \quad (8)$$

$$J_{ij} = \frac{1}{\pi} \int_0^\infty |\widehat{\Psi}(k)|^2 J_0(k|\mathbf{r}_i - \mathbf{r}_j|) k dk, \quad (9)$$

where $N_0 = 2\pi \int_0^\infty \rho(r) r dr$ is the number of particles in a single, isolated condensate.

The oscillating behaviour of the Bessel function, $J_0(kd_{ij})$, brings about the sign change in the coupling constants, J_{ij} , depending on the distance d_{ij} . When J_{ij} is positive the coupling is said to be ferromagnetic and when J_{ij} is negative the coupling is said to be anti-ferromagnetic. We approximate the switching of the coupling sign by $\cos(k_c d + \phi)$, where ϕ is fixed by the system parameters (see Supp. Inf. for the discussion). The state with the phase configuration that carries the highest number of particles in Eq. (8) corresponds to the solution that minimises the XY Hamiltonian, $\mathcal{H}_{XY} = -\sum_{i < j}^n J_{ij} \cos\theta_{ij}$. Between any two polariton condensates the polariton wavefunction forms a standing wave with the density $|\Psi_g|^2 \approx \rho_+ + \rho_- + 2\sqrt{\rho_+ \rho_-} \cos[k_c |x - d_{ij}/2| - k_c |x + d_{ij}/2| - \theta_{ij}]$, where x is the coordinate along

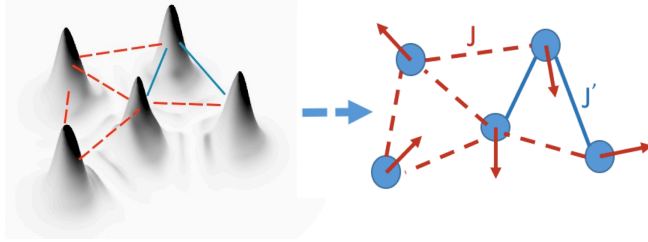


FIG. 1: Schematic of the condensate density map for a five-vertex polariton graph. The sign of the coupling is annotated for some of the edges of the graph: depending on the separation distance between the sites and the outflow wavevector k_c the interactions are either ferromagnetic (solid-blue lines) or anti-ferromagnetic (dashed-red lines). At each vertex \mathbf{r}_i of the graph polaritons have a local phase θ_i that is mapped to a classical vector spin $\mathbf{s}_i = (\cos \theta_i, \sin \theta_i)$.

the line that connects the two nodes separated by a distance d_{ij} and $\rho_{\pm} = \rho(x \pm d_{ij}/2, y)$. Between two polariton condensates the density oscillates proportional to $1 + \cos(2k_c x + \theta_{ij})$, from which the phase difference θ_{ij} of a single shot realization can be extracted directly. For more complex geometries the phase difference can be verified through interferometry and Fourier-space analysis. In Fig. 1 we plot the density of a polariton graph, where for simplicity we have annotated the sign of the coupling for some of the edges of the graph. Depending on the separation distance between the vertices and the outflow wavevector k_c , the interactions are either ferromagnetic (solid-blue lines) or anti-ferromagnetic (dashed-red lines). At each vertex \mathbf{r}_i of the graph polaritons have a local phase θ_i , which in the following we map to a classical vector spin $\mathbf{s}_i = (\cos \theta_i, \sin \theta_i)$ and annotate on top of each vertex as calculated from the minimisation of the XY Hamiltonian.

The Ising polariton chain: we theoretically describe and experimentally address the minimization of the XY Hamiltonian for the simple case of a linear polariton chain with equal spacing $d = d_{ij}$ between neighbours. In the steady state excitation regime, we can calculate the maximum particle number of a polariton dyad as a function of the separation distance, d , by numerically integrating the cGLE to find the solutions of Eqs. (3-4) that maximize N for a given pumping profile $p(\mathbf{r}) = p_0[\exp(-\alpha|\mathbf{r} - \mathbf{d}/2|^2) + \exp(-\alpha|\mathbf{r} + \mathbf{d}/2|^2)]$ of a characteristic width α^{-1} ; the results are shown in Fig. 2(a). The relative phases that realise the maximum particle number switch periodically between 0 and π with the period $2\pi/k_c$ as shown by superimposing the function $\cos(k_c d + \phi)$ in Fig.2(a); we have used the experimental parameters for the pumping profile and k_c as described in “Wavevector Tomography” in

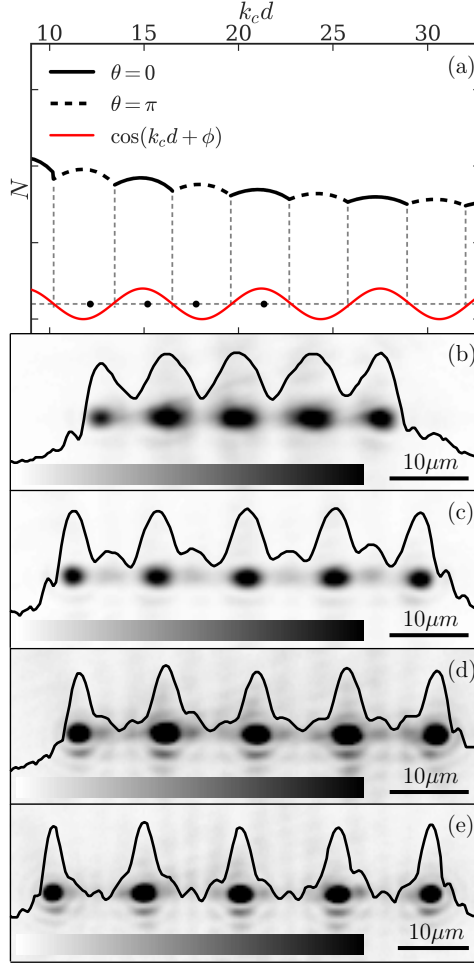


FIG. 2: (a) The maximum number of particles, N , of a polariton condensate dyad formed under incoherent pumping of two nodes as the function of the product $k_c d$ between the nodes obtained by numerical integration of the cGLE for a fixed k_c starting with random initial conditions and choosing the realization that maximizes N . The solid black line corresponds to the maximum number of particles in the in-phase ferromagnetic configuration and the dashed black line to the π -phase difference anti-ferromagnetic configuration. The switching occurs with the periodicity $2\pi/k_c$ as the superimposed graph of $\cos(k_c d + \phi)$ illustrates in red, where $\phi \approx 225^\circ$. (b-e) Experimental realization of an Ising chain of five equidistant polariton nodes with lattice constants of $\sim 9\mu m$, $\sim 11.1\mu m$, $\sim 11.4\mu m$, and $\sim 13.4\mu m$ respectively. The false-grey scale images show the normalised real-space photoluminescence intensity at the energy of the condensate; (b,c) are saturated at 0.7 and (d,e) are saturated at 0.25 to increase the visibility of the low intensity fringes between the nodes. The corresponding $k_c d$ are shown by solid circles on (a).

Supp. Inf. Where the coupling is ferromagnetic (anti-ferromagnetic) the graph of the maximum number of particles is plotted with a solid (dashed) line. We experimentally address an analogue of the Ising chain by injecting a linear chain of five equidistant polariton condensates through non-resonant, continuous wave and spatially modulated optical excitation of a multiple InGaAs quantum well strain compensated semiconductor microcavity [21] that allows for detection of the polariton photoluminescence in the transmission geometry (for the sample description read the “Microcavity sample” and for the description of the excitation/detection scheme read the “Experimental setup” in Supp. Inf.). Figures 2(b-e) show the real-space photoluminescence intensity of the linear chain condensate with increasing lattice constant from $\sim 9\mu m$ to $\sim 13.4\mu m$, at condensation threshold. The relative phase difference realised between neighbours in the chain is either π or zero. The linear chain configuration restricts the spins to two states effectively reducing the chain to the Ising model. The patterns are clearly distinguishable by the number of fringes (density maxima) between the sites: zero or even for anti-ferromagnetic and odd for ferromagnetic coupling. In Fig.2(a) we have annotated the abscissa with solid circles for each of the two separation distances from which the expected sign of coupling is depicted, showing good agreement with the experiment. The observed phase configurations realise the ferromagnetic and anti-ferromagnetic Ising spin chain.

Equidistant vertices across a circle: we consider a geometry of l_N incoherently pumped equidistant polariton vertices positioned on the circumference of a circle. For equal separation distances $d = d_{ij}$ between adjacent sites the XY Hamiltonian to minimise becomes $\mathcal{H}_{XY} = -J \sum_{i=1}^{l_N} \cos(\theta_{i,i+1})$, where $J = J_{ij}$, the summation is cyclic and we took into account only nearest neighbour interactions. If J is positive, then all sites lock in phase ($\theta_{i,i+1} = 0$). If J is negative, the minimum of \mathcal{H}_{XY} occurs for $\theta_{i,i+1} = \pm\pi$, when l_N is even and for $\theta_{i,i+1} = \pm\pi(l_N - 1)/l_N$ when l_N is odd ($l_N > 1$). For odd number of vertices, therefore, the configurations bring about topological vortices of winding $\pm(l_N - 1)/2$, whose properties we explore elsewhere [22]. We experimentally access these regimes through incoherent injection of polaritons at the vertices of a square; Figure 3(a,b,c) show the spin configuration, experimental results of the real-space photoluminescence intensity at the energy of the condensate at condensation threshold and numerical simulations for a square with lattice constants that lead to anti-ferromagnetic, ferromagnetic and the next anti-ferromagnetic coupling respectively. Similar to the Ising polariton chain the type of coupling is clearly

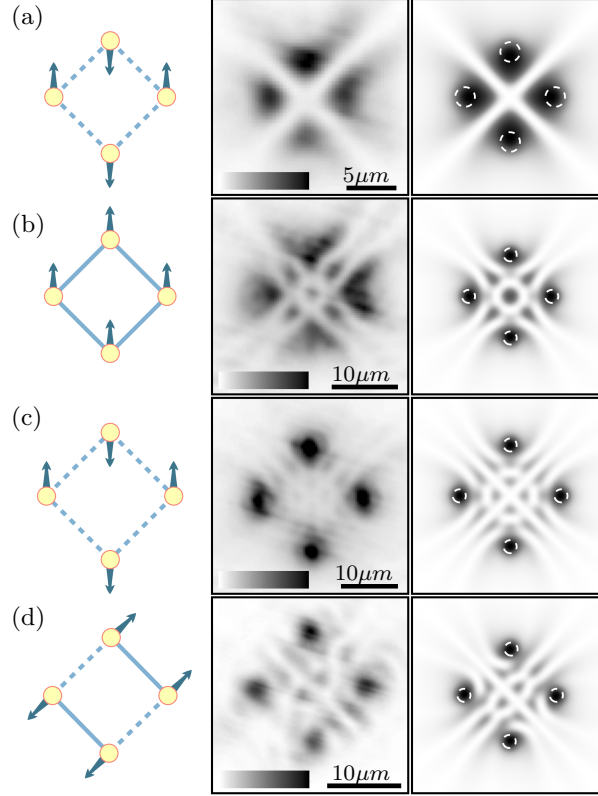


FIG. 3: Spin configurations of square polariton lattices. The diagrams of the numerically calculated spins vectors at the pumping sites $\mathbf{s}_i = (\cos \theta_i, \sin \theta_i)$, the real-space energy tomography of the experimental realisations, and the averaged condensate densities of the numerically simulated condensate wavefunctions for several realizations are shown on the left, central and right columns respectively. Solid and dashed blue lines on the spin vector diagrams (left column) indicate ferromagnetic and anti-ferromagnetic coupling, respectively. The false-grey scale images of the middle column show the normalised real-space photoluminescence intensity at the energy of the condensate at condensation threshold; (c) is saturated at 0.5 to increase the visibility of the low intensity fringes between the vertices. The configurations shown are some elementary building blocks of square lattices such as (a,c) anti-ferromagnetic, (b) ferromagnetic, (d) 90°-compass. The centers of the pumping spots are shown by white dashed circles on the numerical density profiles (right column). The parameters of the numerical simulations of Eqs. (1,2) are listed in the Supp. Inf.

distinguishable by the number and symmetry of fringes between the vertices: zero or even for anti-ferromagnetic (Fig.3(a,c)) and odd for ferromagnetic coupling (Fig.3(b)). These observations are in agreement with the π phase difference reported in Ref.[23]. We can thus

summarise in the case of the square lattice cell that for ferromagnetic coupling polaritons at the vertices lock with zero phase difference and for anti-ferromagnetic coupling polaritons at neighbouring vertices lock with π phase difference.

90° compass model: in the context of solving universal spin models apart from the trivial all ferromagnetic or all anti-ferromagnetic coupling configurations in a square geometry, more complex coupling configurations are of interest. Examples of such configurations are the compass models, where the coupling between the internal spin components is inherently directionally dependent. Such compass-type coupling appears in various physical systems, where the interactions are sensitive to the spatial orientation of the involved orbitals. In polariton graphs the compass models with direction dependent coupling or spin glassy models with random couplings can be realised by changing the pumping intensity and preserving the square geometry, or alternatively, tuning the separation distances so that each vertex has one ferromagnetic and one anti-ferromagnetic coupling with its nearest neighbours. In Fig. 3(c) we have realised the 90° compass model, where each vertex has one ferromagnetic and one anti-ferromagnetic coupling with its neighbours as it is clearly distinguishable by the number of fringes between nearest vertices. The 90° compass, where both ferro- and anti-ferromagnetic coupling appear across the two orthogonal diagonals here, has been proposed as a model to Mott insulators with orbital degrees of freedom and frustrated magnets [24], the plaquette orbital model [25], and the orbital compass model on a checkerboard lattice [26]. Other systems accessible through polariton graphs, include fully random couplings in the square lattice that describe the thermodynamic behaviour of several disordered systems, such as magnetic systems with random Dzyaloshinskii-Moriya interactions [27], disordered Josephson junction arrays [28], disordered substrates [29], and vortex glasses in high- T_c cuprate superconductors [30].

Triangular lattice: the XY Hamiltonian has been simulated on a triangular lattice of atomic condensates discovering a variety of magnetic phases and frustrated spin configurations [31]. In the case of an anti-ferromagnetically coupled polariton triad, arranged at the vertices of an equidistant triangle, the phase configuration that minimizes the XY Hamiltonian corresponds to ± 1 winding ($2\pi/3$ phase difference between the condensates) [18]. Here, we experimentally realise a unit cell of a triangular lattice (rhombus configuration) under incoherent injection of polaritons. Figure 4(a,b,c) show the spin configuration, experimental results of the real-space photoluminescence intensity at the energy of the condensate at con-

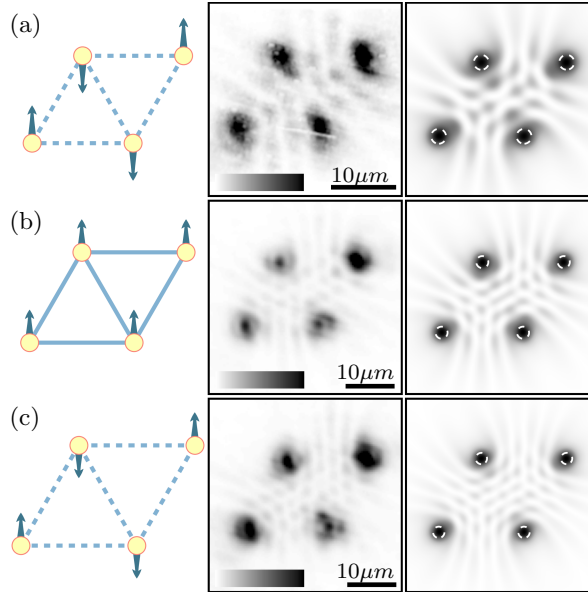


FIG. 4: Spin configurations of the diamond-shaped polariton lattices. The columns of images are as described in the caption to Fig.3. The configurations shown are some elementary building blocks of triangular lattices such as (a,c) anti-ferromagnetic and (b) ferromagnetic rhombuses. The false-grey scale images of the middle column show the normalised real-space photoluminescence intensity at the energy of the condensate at condensation threshold saturated at 0.5 to increase the visibility of the low intensity fringes between the vertices.

condensation threshold and numerical simulation for a rhombus with lattice constants that lead to anti-ferromagnetic, ferromagnetic and the next anti-ferromagnetic coupling, respectively. In the case of ferromagnetic coupling between nearest neighbours and neglecting opposite neighbours interactions across the long diagonal axis of the rhombus, the XY Hamiltonian is minimised at $\mathcal{H}_{XY} \sim -5J$ when all polariton sites lock in phase, as shown in Fig. 4(b). Similarly, in the case of anti-ferromagnetic coupling between nearest neighbours the XY Hamiltonian is minimised at $\mathcal{H}_{XY} \sim 3J$ when there is $\pm\pi$ phase difference between the outer edges of the rhombus. This configuration forces the rhombus in a frustrated state wherein opposite vertices have the same phase. This type of frustrated spin configuration is experimentally realised in Fig. 4(a,c). The corresponding states in Figs. 4(a,b,c) are shown in the order of increasing distance between the sites, therefore, the anti-ferromagnetic states of Figs. 4(a) and 4(c) belong to two different bands of anti-ferromagnetic regions separated by a ferromagnetic band (the alternating anti-ferromagnetic/ferromagnetic couplings bands

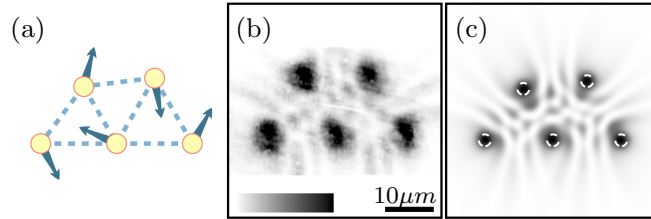


FIG. 5: Spin configurations of a random polariton graph. The panels of images are as described in the caption to Fig.3. The false-grey scale image of the middle column show the normalised real-space photoluminescence intensity at the energy of the condensate at condensation threshold saturated at 0.5 to increase the visibility of the low intensity fringes between the vertices.

are shown in Fig. 2(a)). The measured density profiles show some clear differences: the local minimum at the center of the rhombus along the long diagonal in Fig. 4(a) is replaced by a local maximum in Fig. 4(c).

Random polariton graph: beyond the minimization of the classical XY Hamiltonian of polariton condensates on regular lattices we test our platform on a disordered polariton graph of five vertices. We took a graph initially consisting of a half-hexagon for a lattice constant that leads to anti-ferromagnetic coupling, but with one spot breaking the symmetry. This is achieved experimentally by slightly displacing one spot on the graph. Figure 5 shows the spin configuration, experimental results of the real-space tomography of the photoluminescence intensity at the energy of the condensate at condensation threshold and numerical simulations that correspond to this graph. For the symmetric configuration of a half-hexagon and considering only nearest neighbours interactions, the XY Hamiltonian is minimised at $\mathcal{H}_{XY} \sim 3.86J$ with an alternating winding around each cell slightly deviating from $2\pi/3$ difference reported for a single equilateral triangle (see Supp. Inf. for details). Breaking the symmetry leads to a different phase distribution, while maintaining the winding around each cell. The analysis of the fringes on the experimental image (with the different rows of local maxima along the two long diagonals) shows that the symmetry is explicitly broken.

Extended polariton lattices: in the following we explore the potential of the polariton simulator in finding the global minimum of the XY Hamiltonian with increasing the number of vertices on a square lattice. Figure 6(a,b,c) shows the experimental results of the normalised real-space photoluminescence intensity at the energy of the condensate at condensa-

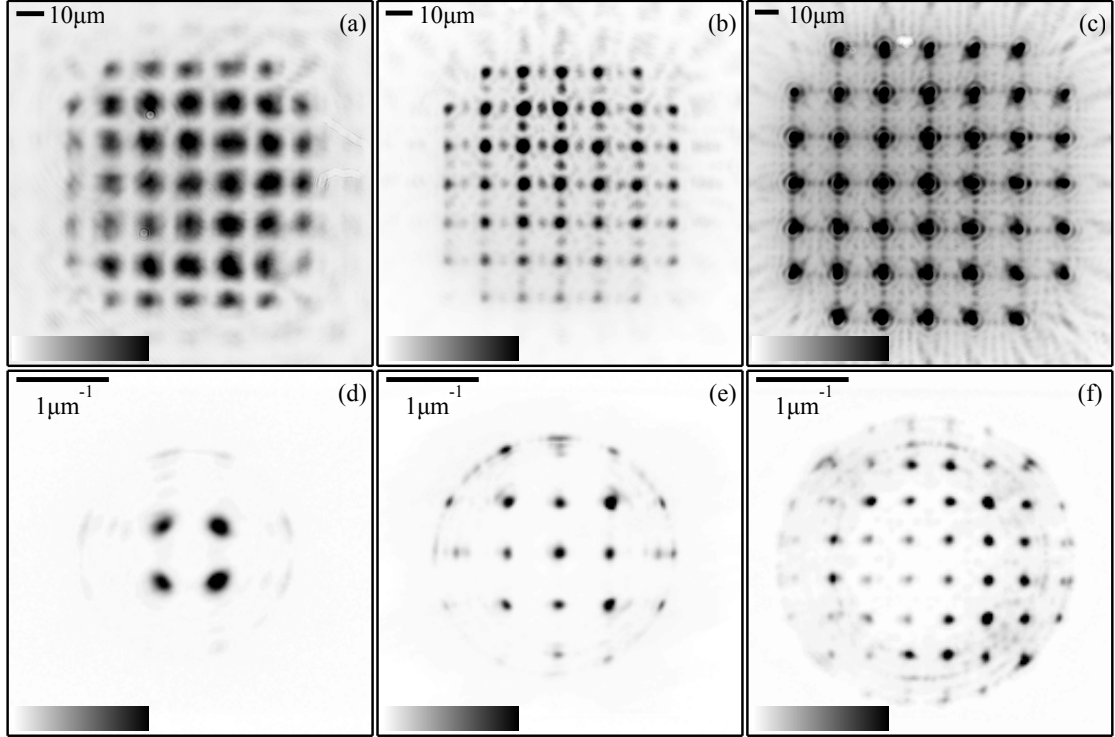


FIG. 6: The first row shows the normalised real-space photoluminescence intensity at the energy of the condensate at condensation threshold in a false-greyscale for (a,c) anti-ferromagnetic and (b) ferromagnetic configuration of 45 coherently coupled polariton condensates arranged at the vertices of a square lattice; (a) is saturated at 0.7 and (b,c) are saturated at 0.3 to increase the visibility of the low intensity fringes between the vertices. The second row shows the normalised photoluminescence intensity of the two-dimensional Fourier-space corresponding to the lattices of (a-c) at the energy of the condensate at condensation threshold in a false-greyscale; (a,b) are saturated at 0.5 and (c) is saturated at 0.3 to increase the visibility of the low intensity coherent spots.

tion threshold for 45 coherently coupled polariton condensates arranged at the vertices of a square lattice. The lattice constants chosen here result in anti-ferromagnetic, ferromagnetic and next anti-ferromagnetic coupling respectively. Figure 6(d,e,f) shows the corresponding normalised photoluminescence intensity of the two-dimensional Fourier-space corresponding to the lattices of Fig.6(a-c) at the energy of the condensate at condensation threshold. The contrast of the interference pattern observed in the Fourier-space images is indicative of the degree of coherence across the lattice. In particular, the low intensity centre surrounded by

sharp intense “Bragg peaks” in Fig.6(d,f) indicates anti-ferromagnetic coupling, whereas the high intensity centre in the two-dimensional Fourier-space of Fig.6(e) indicates ferromagnetic coupling. We find that in the steady-state excitation regime and for the number of vertices that we are technically capable to realise, -up to 45 here-, the injected square polariton lattices always condense with the phase configuration that corresponds to the ground state of the bespoke XY Hamiltonian.

Discussion and conclusions: Unlike a proposal for a quantum computer that is intended as a universal platform, analogue simulators are proposed to solve specialized classes of problems suited for the architecture and capabilities of the underlying physical system. For example the intensely investigated superconducting quantum bits platform intends to simulate the Ising model with transverse fields through the quadratic unconstrained binary optimization model (QUBO) [32]. Trapped ions were used to simulate Ising, XY , and XYZ interactions between effective spins [33]. Another scalable platform that benefits from high temperature operation is the coupled degenerate OPOs Ising Machine, which solves the MAX-CUT [34, 35]. Our polariton platform simulates the XY model, which can be formulated as a quadratic non-convex constrained optimization model (QNCO). The hardest instances of all mentioned problems are in the NP-hard classical complexity class of problems. QUBO or MAX-CUT can be mapped into QNCO and vice versa but with a huge overhead on the number of nodes [7]. Therefore, assuming that all platforms eventually show better than classical computer behavior it is likely that each platform will be used to address its own type of problems. Most relevant platforms addressing the XY Hamiltonian for a large number of spins are the optical lattices of atomic condensates [31] and the photon lasers networks [36]. Whereas both are scalable, they are likely to reach a local rather than the global minimum of the Hamiltonian. In both the photon laser and polariton platform, the phase configuration of the lasers or the condensates, at the threshold, corresponds to the global minimum of the energy landscape. In the case of the polariton platform, it is possible to operate in the steady state regime at threshold, and as we have demonstrated experimentally, achieve the global minimum of the XY Hamiltonian; photon laser systems that operate stably well above threshold are described by the Kuramoto model and can be trapped in local minima of the energy landscape. In the configurations we considered so far, the energy gap between the ground and excited states is larger than the linewidth and that allows for the ground state to be accurately found. Further work is needed to establish how

the energy gap relates to the linewidth in more general lattice configurations. Clearly for the polariton simulator introduced here, more work also is needed to determine the fundamental computation power, the upper limit on the number of coherently coupled vertices and level of connectivity. Nevertheless, the optical approach of imprinting two-dimensional polariton lattices of arbitrary geometries and density profiles allows for tunable coupling strengths between vertices and as we have demonstrated it offers the potential for rapid scalability utilising mature semiconductor and photonic technologies.

-
- [1] Pierce, N.A. and Winfree, E. Protein Design is NP-hard. *Protein Engineering*, **15**, 779 (2002).
 - [2] Durlauf, S.N. How can statistical mechanics contribute to social science? *Proc. Natl. Acad. Sci. U.S.A.*, **96**, 10582 (1999).
 - [3] Rojas, R. Neural Network—A Systematic Introduction, Springer-Verlag, (1996).
 - [4] Shehory, O. and Kraus, S. Methods for task allocation via agent coalition formation. *Artificial Intelligence*, **101**, 165 (1998).
 - [5] Ghiringhelli, L.M. et al Big Data of Materials Science: Critical Role of the Descriptor. *Phys. Rev. Letts.*, **114**, 105503 (2015)
 - [6] Balents, L. Spin liquids in frustrated magnets. *Nature* **464**, 199 (2010)
 - [7] Cuevas, G. D. and Cubitt, T. S. Simple universal models capture all classical spin physics. *Science* **351**,1180 (2016)
 - [8] Woeginger, G. J. Exact Algorithms for NP-Hard Problems: A Survey. *Combinatorial Optimization*, **2570** Lecture Notes in Computer Science, 185 (2003).
 - [9] Lucas, A., Ising formulations of many NP problems. *Front. Phys.*, **2**, 1 (2014)
 - [10] Barahona, F. On the computational complexity of Ising spin glass models *J. Phys. A* **15**, 3241 (1982).
 - [11] Georgescu, I. M., Ashhab, S. & Nori, F. Quantum simulation. *Rev. Mod. Phys.* **86**, 153 (2014).
 - [12] Zhang, S. & Huang, Y. Complex quadratic optimization and semidefinite programming. *SIAM J. Optim.*, **16** 871 (2006)
 - [13] Man-Cho So, A., Zhang, J., & Ye, Y. On approximating complex quadratic optimization problems via semidefinite programming relaxations. *Math. Program., Ser. B*, Springer, (2005).
 - [14] Berezinskii, V. L. Destruction of long-range order in one-dimensional and two-dimensional

- systems having a continuous symmetry group I. Classical systems. *Sov. Phys. JETP* **32**, 493 (1971).
- [15] Kosterlitz, J. M. & Thouless, D. J. Ordering, metastability and phase transitions in two-dimensional systems. *J. Phys. C* **6**, 1181 (1973).
- [16] Weisbuch, C., Nishioka, M., Ishikawa, A. & Arakawa, Y. Observation of the coupled exciton-photon mode splitting in a semiconductor quantum microcavity. *Phys. Rev. Lett.* **69**, 3314 (1992)
- [17] Kasprzak, J. *et al.* Bose-Einstein condensation of exciton polaritons. *Nature* **443**, 409 (2006).
- [18] Ohadi, H. *et al.* Non-trivial phase coupling in polariton multiplets. *Phys. Rev. X* **6**, 031032 (2016).
- [19] Wouters, M. & Carusotto, I. Excitations in a nonequilibrium Bose-Einstein condensate of exciton polaritons. *Phys. Rev. Lett.* **99**, 140402 (2007).
- [20] Keeling, J. & Berloff, N. G. Spontaneous rotating vortex lattices in a pumped decaying condensate. *Phys. Rev. Lett.* **100**, 250401 (2008).
- [21] Cilibrizzi, P. *et al.* Polariton condensation in a strain-compensated planar microcavity with InGaAs quantum wells. *Appl. Phys. Lett.* **105**, 191118 (2014).
- [22] Kalinin, K., Silva, M., Langbein, W., Berloff, N.G., Lagoudakis, P.G. Spontaneous discrete vortex solitons in polariton lattices. In preparation (2016)
- [23] Tosi, G. *et al.* Geometrically locked vortex lattices in semiconductor quantum fluids. *Nat. Comm.*, **3**, 1243 (2012).
- [24] Nussinov, Z. & van den Brink, J. Compass models: theory and physical motivations. *Rev. Mod. Phys.* **87**, 1 (2015).
- [25] Biskup, M. & Kotecky, R. True nature of long-range order in a plaquette orbital model. *J. Stat. Mech.* **11**, 11001 (2010).
- [26] Nasu, J. and Ishihara, S. Orbital compass model as an itinerant electron system. *Europhysics Letters* **97**, 27002 (2012).
- [27] Rubinstein, M., Shraiman, B. & Nelson, D. R. Two-dimensional XY magnets with random Dzyaloshinskii-Moriya interactions. *Phys. Rev. B* **27**, 1800 (1983).
- [28] Granato, E. & Kosterlitz, J. M. Disorder in Josephson-junction arrays in a magnetic field. *Phys. Rev. Lett.* **62**, 823 (1989).
- [29] Cha, M.C. & Fertig, H. A. Orientational order and depinning of the disordered electron solid.

- Phys. Rev. Lett.* **73**, 870 (1994).
- [30] Gingras, M. J. P. & Huse, D. A. Topological defects in the random-field XY model and the pinned vortex lattice to vortex glass transition in type-II superconductors. *Phys. Rev. B* **53**, 15193 (1996).
- [31] Struck, J. Quantum simulation of frustrated classical magnetism in triangular optical lattices. *et al. Science* **333**, 996 (2011).
- [32] Johnson M.W., et al. Quantum annealing with manufactured spins. *Nature*, **473**, 194 (2011)
- [33] Porras, D., and Cirac, J.I. Effective Quantum Spin Systems with Trapped Ions. *Phys. Rev. Letts.* **92**, 207901 (2004)
- [34] Utsunomiya, S., Takata, K. & Yamamoto, Y. Mapping of Ising models onto injection-locked laser systems. *Opt. Express* **19**, 18091 (2011).
- [35] Marandi, A., Wang, Z., Takata, K., Byer, R. L. & Yamamoto, Y. Network of time-multiplexed optical parametric oscillators as a coherent Ising machine. *Nature Photonics* **8**, 937-942 (2014).
- [36] M. Nixon, E. Ronen, A. A. Friesem, and N. Davidson, Observing geometric frustration with thousands of coupled lasers, *Phys. Rev. Lett.* **110**, 184102 (2013).

Methods

Methods are available within the supplementary information in the online version of this paper.

Acknowledgements

The authors acknowledge the support of the Skoltech NGP Program (Skoltech-MIT joint project), and the UK's Engineering and Physical Sciences Research Council (grant EP/M025330/1 on Hybrid Polaritonics). N.G.B. is grateful to Professor Nikolai Prokof'ev for fruitful discussions.

Author contributions

N.G.B and P.G.L. designed the research and wrote the paper. M.S., A.A. and P.G.L performed the experiments. M.S., and P.G.L analysed the experimental data. N.G.B. and

K.K. performed theoretical modelling. K.K performed numerical simulations and analysis of numerical data. J.D.T and P.C. contributed to the experimental apparatus and complementary measurements. W.L. and P.G.L designed and managed the growth of the sample.

Additional information

The authors declare no competing financial interests. Reprints and permission information is available online at www.nature.com/reprints. Correspondence and requests for materials should be addressed to N.G.B. and P.G.L. The data from this paper can be obtained from the University of Southampton ePrints research repository: <http://doi.org/10.5258/SOTON/D0124>